Acta Pharmaceutica Sinica B 2024;14(6):2685–2697

Chinese Pharmaceutical Association
Institute of Materia Medica, Chinese Academy of Medical Sciences

Acta Pharmaceutica Sinica B

www.elsevier.com/locate/apsb
www.sciencedirect.com

ORIGINAL ARTICLE

Precise nano-system-based drug delivery and synergistic therapy against androgen receptor-positive triple-negative breast cancer

Fangyan Gao[a,†], Yueyao Wu[b,†], Runtian Wang[a,†], Yuhui Yao[c], Yiqiu Liu[a], Lingling Fan[a], Jingtong Xu[a], Jian Zhang[d,*], Xin Han[b,*], Xiaoxiang Guan[a,e,*]

[a]*Department of Oncology, the First Affiliated Hospital of Nanjing Medical University, Nanjing 210029, China*
[b]*Jiangsu Collaborative Innovation Center of Chinese Medicinal Resources Industrialization, School of Medicine & Holistic Integrative Medicine, Nanjing University of Chinese Medicine, Nanjing 210023, China*
[c]*Department of Oncology, the Second Hospital of Nanjing, Nanjing University of Chinese Medicine, Nanjing 210023, China*
[d]*Department of Medical Oncology, Fudan University Shanghai Cancer Center, Shanghai 200032, China*
[e]*Jiangsu Key Lab of Cancer Biomarkers, Prevention and Treatment, Collaborative Innovation Center for Cancer Personalized Medicine, Nanjing Medical University, Nanjing 211166, China*

Received 25 December 2023; received in revised form 8 February 2024; accepted 16 February 2024

KEY WORDS

Triple-negative breast cancer;
Androgen receptor;
Checkpoint kinase 1;
Enzalutamide;
MK-8776;
Synergy;
$HMnO_2$;
Nanodrug delivery system

Abstract Targeting androgen receptor (AR) has shown great therapeutic potential in triple-negative breast cancer (TNBC), yet its efficacy remains unsatisfactory. Here, we aimed to identify promising targeted agents that synergize with enzalutamide, a second-generation AR inhibitor, in TNBC. By using a strategy for screening drug combinations based on the Sensitivity Index (SI), we found that MK-8776, a selective checkpoint kinase1 (CHK1) inhibitor, showed favorable synergism with enzalutamide in AR-positive TNBC. The combination of enzalutamide and MK-8776 was found to exert more significant anti-tumor effects in TNBC than the single application of enzalutamide or MK-8776, respectively. Furthermore, a nanoparticle-based on hyaluronic acid (HA)-modified hollow-manganese dioxide ($HMnO_2$), named HMnE&M@H, was established to encapsulate and deliver enzalutamide and MK-8776. This HA-modified nanosystem managed targeted activation *via* pH/glutathione responsiveness. HMnE&M@H repressed tumor growth more obviously than the simple addition of enzalutamide and

*Corresponding authors.
E-mail addresses: syner2000@163.com (Jian Zhang), xhan0220@njucm.edu.cn (Xin Han), xguan@njmu.edu.cn (Xiaoxiang Guan).
†These authors made equal contributions to this work.

Peer review under the responsibility of Chinese Pharmaceutical Association and Institute of Materia Medica, Chinese Academy of Medical Sciences.

https://doi.org/10.1016/j.apsb.2024.03.012

MK-8776 without a carrier. Collectively, our study elucidated the synergy of enzalutamide and MK-8776 in TNBC and developed a novel tumor-targeted nano drug delivery system HMnE&M@H, providing a potential therapeutic approach for the treatment of TNBC.

1. Introduction

Breast cancer stands as the most prevalent cancer in women and contributes significantly to cancer-related fatalities[1]. It is categorized into three primary subtypes based on the expression of estrogen receptor (ER), progesterone receptor (PR), and human epidermal growth factor receptor 2 (HER2/ErbB2): hormone receptor-positive, HER2-enriched, and triple-negative breast cancer (TNBC)[2]. TNBC is a highly invasive and aggressive subtype that lacks specific therapeutic agents compared with hormone receptor-positive and HER2-enriched breast cancer. Moreover, over 30% of TNBC patients are diagnosed with distant metastases within five years of initial diagnosis[3,4]. Without the option of hormone therapies against ER, PR, or targeted drugs against ErbB2, current options for early-line treatment of advanced TNBC were mainly based on systematic administration of conventional cytotoxic chemotherapy[5,6], and only a few targeted therapies have been approved available for a partial TNBC population[7]. Nevertheless, the diverse side effects, such as gastrointestinal dysfunction and myelosuppression, severely limit the efficiency of chemotherapy[8,9]. An alternative therapeutic strategy for treating TNBC is highly desirable in clinical practice, thus improving therapeutic efficacy and reducing adverse side effects.

Although TNBC does not have hormone receptors typically found in other types of breast cancer, approximately 10−15% of TNBC patients express the androgen receptor (AR)[10]. Recent investigations have highlighted the significant impact of AR on TNBC's tumorigenic qualities[11]. Following the development of next-generation anti-androgens for the treatment of prostate cancer, hormonal therapy targeting AR in the fraction with AR^+ TNBC has regained interest and represents a new therapeutic option for these patients[12-15]. Bicalutamide was utilized in a phase II clinical trial to treat patients with AR^+ TNBC, and around 19% of patients obtained clinical benefits from the inhibition of AR[16]. Enzalutamide, a second-generation AR inhibitor, has greater anti-cancer activity compared to first-generation AR inhibitors (such as bicalutamide) because of its improved AR affinity and stronger inhibition of AR nuclear translocation[17-19]. Recently, another phase II study investigated the anti-cancer efficacy and safety of enzalutamide in patients with locally progressed or metastatic AR^+ TNBC. About 30% of patients exhibited clinical benefits after 24 weeks of medication, showing promising clinical efficacy and good tolerance[20]. Despite the application of enzalutamide in AR^+ TNBC, which has achieved optimistic research results, the overall response rate is still unsatisfactory due to adaptive resistance and subsequent tumor progression.

Numerous targeted medications have been incorporated into combination regimens to combat or postpone resistance to endocrine therapy. These include cell cycle inhibitors, histone deacetylase (HDAC) inhibitors, and inhibitors targeting the phosphatidylinositol three kinase-protein kinase B-mammalian target of rapamycin (PI3K−AKT−mTOR) pathway[21]. The PALOMA-2 trial suggested the synergistic application of palbociclib, a cell cycle inhibitor, alongside endocrine therapy, contributing to a longer progression-free survival (PFS) for patients with ER-positive breast cancer[22]. Inspired by the synergistic treatment of ER-positive breast cancer, we sought to explore whether cell cycle inhibitors and anti-hormone agents could be applied to AR^+ TNBC. However, few studies about the combination of AR inhibitors and targeted drugs have been reported. Given that AR blockade could activate cell cycle signaling, simultaneous suppression of both AR and cell cycle progression is worthy of investigation[23,24]. Therefore, we selected a drug library composed of multiple cell cycle inhibitors to test whether these drugs have a synergistic effect with enzalutamide in the treatment of TNBC. Furthermore, in order to maximize the effectiveness of combination medications, a nano drug delivery system that can overcome biological barriers in tumors is a promising candidate for drug delivery[25]. The nano drug delivery systems are based on nanomaterials with a size around 100 nm, exhibiting surface effects and small size effects[26]. Differing from traditional drugs, nano-drug delivery systems have many advantages, including excellent solubility, outstanding bioavailability, and fewer adverse effects[27]. Among them, hollow manganese dioxide ($HMnO_2$) is an ideal nanocarrier for loading a variety of agents due to its low toxicity, remarkable response to tumor microenvironment (TME), and high loading capacities[28,29].

Herein, we found that the combination of enzalutamide and MK-8776 had synergic effects in TNBC. Accordingly, we developed an $HMnO_2$-based nano platform that encapsulates both enzalutamide and MK-8776 and is further coated with hyaluronic acid (HA), termed $HMnO_2$-Enzalutamide-MK-8776@HA (HMnE&M@H), thereby providing a prospective therapeutic option for the treatment of AR^+ TNBC.

2. Materials and methods

2.1. Cell culture and transfection

The breast cancer cell lines Hs578T, BT549, and 4T1 were purchased from the Typical culture preservation center (ATCC, USA). Hs578T and 4T1 cells were cultured using DMEM medium (Gibco, CA, USA). RPMI 1640 medium (Gibco, CA, USA) was used to culture BT549 cells. Both DMEM and RPMI1640 media were added with 10% fetal bovine serum (FBS) and 1% penicillin/streptomycin. An additional 0.023 IU/mL insulin was added to the medium for BT549 cells. All cells were cultured at a temperature of 37 °C in a humidified atmosphere with 5% CO_2. The overexpression plasmid of RAD51 was designed and synthesized by Genepharma (Shanghai, China). The lipofectamine 3000 (ThermoFisher, MA, USA) was utilized for cell transfection according to the manufacturer's protocol.

2.2. Cell counting kit 8 (CCK-8) assay

Cell viability was measured using the CCK-8 assay (HY−K0301, MedChemExpress, MA, USA). In brief, cells were seeded at a density of 2000 cells per well in a 96-well plate. After 24 h, the cells were treated with different drugs. The CCK-8 solution (10 μL) was added to each well 48 h later, and the 96-well plates were then incubated at 37 °C for another hour. The microplate reader was used to record the absorbance at 450 nm.

2.3. MTT assay

The effect of this nano drug delivery system on cell growth was measured using MTT assay. In brief, following treatment, cells were incubated with MTT (HY-15924, MedChemExpress, MA, USA) in the dark for 4 h, after which measurements were taken using a microplate reader.

2.4. Drug combination screening

Enzalutamide (#S1250), MK-8776(#S2735), and an inhibitor drug library containing 121 cell cycle small molecule inhibitors (#L5100) were purchased from Selleck Chemical Company (Shanghai, China). TNBC cells were treated with DMSO (0.2%), enzalutamide (20 μmol/L in Hs578T, 50 μmol/L in BT549), a drug library agent (1 μmol/L), and a combination of enzalutamide with each agent. After 48 h, each well was added with 10 μL CCK-8 solution, and cells were incubated at 37 °C for an additional hour. The absorbance at 450 nm was measured. Using the calculation formula for the SI value (Fig. 1A), the SI value was determined, and drugs exhibiting synergistic effects when combined with enzalutamide were screened.

2.5. Cell migration and invasion assays

Transwell chambers (Millipore, HE, Germany), either pre-coated with matrigel or left uncoated, were utilized for conducting migration and invasion experiments. TNBC cells (1×10^5 cells/chamber), suspended in a serum-free medium, were seeded into the upper chamber, while the lower chamber was filled with a complete medium containing 10% FBS. Following an incubation period of 24−48 h at 37 °C, cells that migrated through the membrane were fixed with 4% paraformaldehyde (Solarbio, Beijing, China) and subsequently stained with crystal violet (C0121, Beyotime, Nanjing, China). Cell counting was then performed using an inverted microscope.

2.6. Wound healing

TNBC cells were seeded into 6-well plates and allowed to adhere fully. A wound was created in the middle of the plates by scraping the cell. Subsequently, the medium was replaced with a serum-free medium. The fraction of cell coverage along the wound line was calculated after 24 h of incubation.

2.7. Western blotting

The cells were lysed in the RIPA buffer (P0013B, Beyotime, Nanjing, China), and then they were fully lysed using ultrasound. A BCA protein detection kit (P0009, Beyotime, Nanjing, China) was employed for the detection of protein concentration. Protein samples were separated using 6%−10% SDS-PAGE gel and subsequently transferred to PVDF membranes. The membranes were blocked with 5% fat-free milk for 2 h. Subsequently, primary antibodies were used to incubate the membranes overnight at 4 °C. Corresponding secondary antibodies were then used for an additional 1 h of incubation. Ultimately, a chemiluminescence system was used to detect the signal. The primary antibodies anti-AR (1:2000, ab108341), anti-γ-H2AX (1:1000, ab22551), anti-RAD51 (1:10,000, ab133534), anti-DNA PKcs (1:1000, ab32566), anti-RAD50 (1:1000, ab208019), anti-BAX (1:1000, ab32503), anti-BCL-2 (1:1000, ab182858), anti-E-cadherin (1:1000, ab231303), anti-Vimentin (1:1000, ab92547), anti-MMP-9 (1:1000, ab76003), anti-MMP-2 (1:1000, ab92536), and anti-GAPDH (1:1000, ab8245) were provided by Abcam (MA, USA), while anti-CHK1 (1:1000, #2360), and anti-p-CHK1 (1:1000, #90178) were obtained from Cell Signaling Technology (MA, USA).

2.8. Flow cytometry

The cell cycle and apoptosis were assessed by flow cytometry analysis. For cell cycle detection, cells were harvested and washed with cold PBS triple times. Afterward, cells were fixed with 70% ethanol, treated with RNaseA, and stained with propidium iodide (PI). For cell apoptosis analysis, cells were resuspended in an annexin V binding buffer, and FITC-conjugated annexin V and PI were added for a 15-min incubation at room temperature. Finally, flow cytometry (FACScan, BD Biosciences, NJ, USA) was applied for the detection of cell cycle and apoptosis, and the data was analyzed by FlowJo software (version 10.8.1, BD Biosciences, NJ, USA).

2.9. Synthesis of nanoparticles

Firstly, monodisperse silica nanoparticles were synthesized with tetraethyl orthosilicate (TEOS). To get the silica nanoparticles, a mixture of 26 mL water and 13 mL ethanol was prepared, followed by the addition of 1.3 mL ammonia water and 1.4 mL TEOS. Subsequently, 0.2 g resorcin and 0.3 mL formaldehyde were added to the mixture, which was stirred for 12 h. After centrifugation, SiO_2@RF was obtained. Next, 0.4 g potassium permanganate solution was added to the SiO_2@RF solution, and an ultrasonic reaction was conducted at a low temperature for 6 h. After centrifugal cleaning two times, sodium hydroxide solution was added, and the solution reacted in an 80 °C water bath for 6 h. The resulting solution was centrifuged and washed to obtain the product $HMnO_2$. To synthesize HMnE&M@H, MK-8776 and enzalutamide were added to the $HMnO_2$ solution (1 mg/mL) and stirred at room temperature overnight. The sample was then centrifuged at 10,000 rpm (5804, Eppendorf, HH, Germany) to discard the supernatant. The collected precipitate was resuspended with ddH_2O and dispersed using sonication. After another round of centrifugation, the resulting precipitate was referred to as nanoparticles HMnE&M. Subsequently, a 0.5 mg/mL HA solution was introduced to resuspend the nanoparticles, and the mixture was stirred for 1 h. After another round of centrifugation, the retained precipitate mainly represented HMnE&M@H.

2.10. Immunofluorescence staining

For immunofluorescence staining, cells were fixed by using 4% paraformaldehyde. Afterward, cells were exposed to 0.5% Triton X-100 for 30 min and 3% H_2O_2 for 5 min at room temperature. The immunofluorescence blocking reagent (Beyotime, Nanjing,

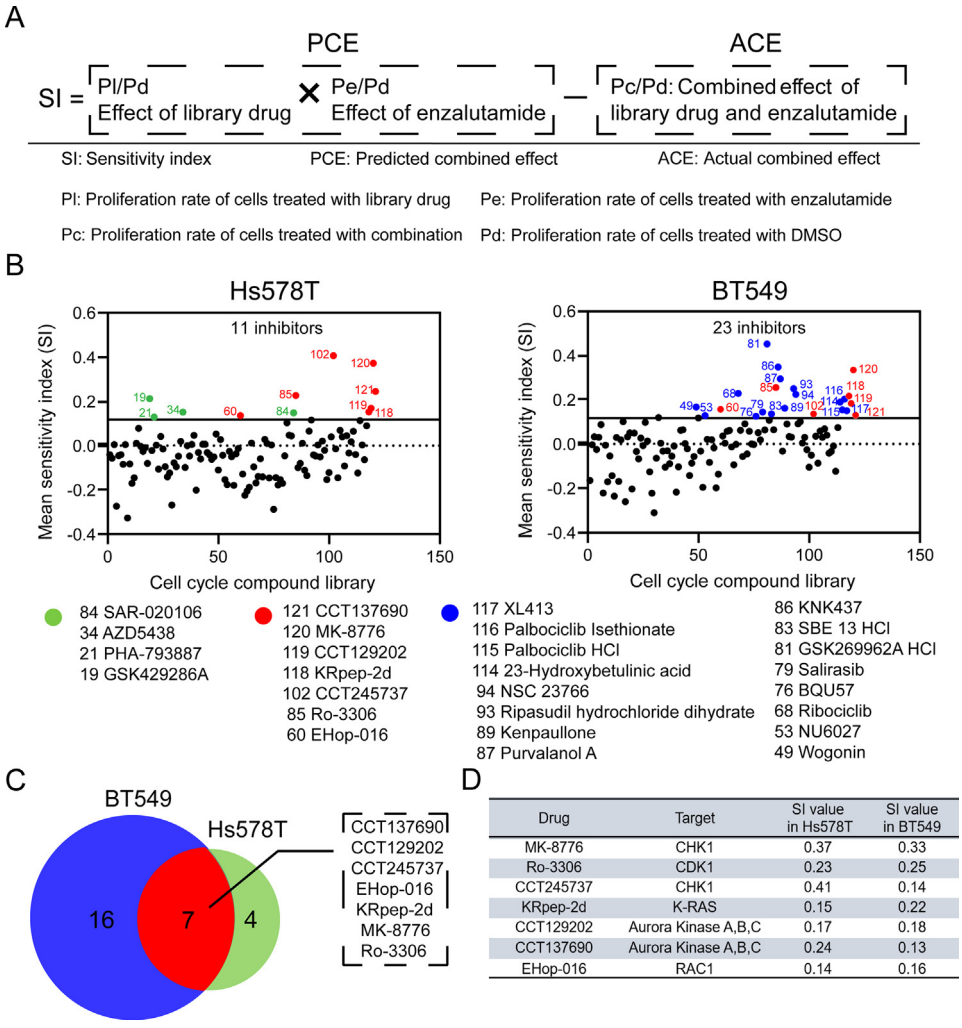

Drug	Target	SI value in Hs578T	SI value in BT549
MK-8776	CHK1	0.37	0.33
Ro-3306	CDK1	0.23	0.25
CCT245737	CHK1	0.41	0.14
KRpep-2d	K-RAS	0.15	0.22
CCT129202	Aurora Kinase A,B,C	0.17	0.18
CCT137690	Aurora Kinase A,B,C	0.24	0.13
EHop-016	RAC1	0.14	0.16

Figure 1 Combined drug screening identified compounds exerting synergistic anti-tumor effects with enzalutamide in TNBC. (A) Formula to calculate the SI value for identification of prospective targeted drugs that enhance enzalutamide's anti-TNBC effects. (B) The scatter plot displays the number of inhibitors that have been found to have potent synergistic effects with enzalutamide. The standard of strong synergy is SI $\geq$ 0.12. The green dots represent the drugs that have synergistic effects with enzalutamide only in Hs578T cells, the blue dots show the drugs that have synergistic effects with enzalutamide only in BT549 cells, and the red dots display the drugs that have synergistic effects with enzalutamide in both two cells. (C) and (D) Seven candidates were listed in Hs578T and BT549, respectively, after testing the synergistic effect of combination drugs.

China) was used to block cells for another 30 min. Finally, DAPI regent (0100-20, SouthernBiotech, AL, USA) was added to stain nuclear. The fluorescence was observed under the laser confocal microscope (LSM700, ZEISS, BW, Germany).

2.11. *Animal models*

Female BALB/c mice, aged four weeks, were obtained from Nanjing Meiris Biotechnology Co., Ltd. The Animal Care and Use Committee of Nanjing Medical University (Ethics Approval Number: IACUC-2211003) approved the animal experiments, and all the experiments were performed according to the Guide for the Care and Use of Laboratory Animals. Mice were injected with 4T1 cells (1×10^6) subcutaneously and received treatment when the tumor volume reached 60 mm^3. In brief, 36 mice were divided into six distinct treatment groups randomly: PBS, HMn@H, HMnE@H (20 mg/kg enzalutamide), HMnM@H (5 mg/kg MK-8776), E&M (20 mg/kg enzalutamide + 5 mg/kg MK-8776), and HMnE&M@H (20 mg/kg enzalutamide + 5 mg/kg MK-8776). Treatments were administered every other day for two weeks. Besides, female BALB/c mice aged six weeks were used for establishing the breast cancer lung metastasis models by intravenously injecting 5×10^5 4T1 cells. These mice were randomly assigned to receive interventions of PBS, E&M, and HMnE&M@H.

2.12. *In vivo imaging*

Using the IVIS Spectrum, fluorescence imaging was performed *in vivo*. HMnE&M@H and HMnE&M nanoparticles were modified with the fluorescent dye Cy7 and then administrated to 4T1 tumor-bearing mice *via* the caudal vein. Visible light imaging was

performed at 1, 4, 8, and 24 h after injection. After 24 h, fluorescence imaging was performed on tumor tissues and major organs *in vitro*. The 4T1 tumor-bearing mice were given HMnE&M@H nanoparticles through the caudal vein, and MR imaging was carried out at 0 and 4 h after injection using a small animal nuclear magnetic resonance imager (Biospec 7T/20 USR, Bruker, MA, USA).

2.13. Hematoxylin and eosin (H&E) and immunohistochemical (IHC) staining

Major organs and tumors were removed from the mice and fixed in formalin. The treated tissues were subsequently paraffin-embedded and sliced into tiny pieces, followed by staining with H&E. Formalin-fixed xenograft tumor samples were utilized for IHC staining to assess the expression of γ-H2AX and Ki-67. Briefly, tissues underwent dehydration in various concentrations of ethanol solutions, followed by three changes of xylene for clearing, and were then embedded in heated paraffin (56−58 °C). Tissue samples were embedded in paraffin and then cut into 4 to 6-mm slices. Deparaffinization and rehydration were performed prior to staining. Antigen retrieval was performed using citrate antigen retrieval solution (Beyotime, Nanjing, China) according to the manufacturer's protocol. To inhibit endogenous hydrogen peroxidase activity, 3% H_2O_2 was applied for 10 min, followed by rinsing with PBS. The slides were then treated with appropriate primary antibodies, including anti-γ-H2AX (1:200, ab22551, Abcam, MA, USA) and anti-Ki-67 (1:200, ab16667, Abcam, MA, USA). Beyotime (Nanjing, China) provided the secondary antibodies against mice or rabbits.

2.14. Statistical analysis

GraphPad Prism 7.0 software (San Diego, CA, USA) was applied for statistical analysis, and the results are presented as the mean ± SD. The two medication combinations' isobologram was analyzed using the CompuSyn 2.0 program (ComboSyn, NJ, USA)[30]. The variables of the two groups were compared using the two-tailed Student's *t*-test, and ANOVA was used for comparisons across multiple groups. Statistics were considered significant when P values were below 0.05.

3. Results

3.1. Combined drug screening identified compounds exerting synergistic anti-tumor effects with enzalutamide in TNBC

The expression level of AR protein in five TNBC cell lines was detected first. Hs578T and BT549 cell lines were chosen for further study because of the higher expression level of AR protein compared to others (Supporting Information Fig. S1). We refer to the high-throughput drug combination screening method and introduce the Sensitivity index (SI) score to evaluate the impact of synergies[31]. The SI score refers to the difference between the predicted and actual combined effects. The proliferation rate of cells treated with DMSO was applied as the internal control (Pd). The predicted combined effect (PCE) is the product of the relative proliferation rate of cells treated with enzalutamide (Pe) and a library drug (Pl). The actual combined effect (ACE) was the relative proliferation rate of cells treated with enzalutamide in combination with a certain library drug (Pc, Fig. 1A). The working dose of enzalutamide was determined *via* CCK-8 assay at first, and the results demonstrated that the appropriate concentration of enzalutamide in Hs578T was 20 μmol/L, and 50 μmol/L in BT549 cells (Supporting Information Figs. S2A and S2B). In order to calculate the SI score for each drug in the library, Hs578T cells were treated as follows: DMSO, 20 μmol/L enzalutamide, 1 μmol/L library drug, and the combination of 20 μmol/L enzalutamide and 1 μmol/L library drug. Similarly, the following treatments were applied to BT549 cells: DMSO, 50 μmol/L enzalutamide, 1 μmol/L library drug, and the combination of 50 μmol/L enzalutamide and 1 μmol/L library drug. An SI score ranging from 0 to 1 indicates a synergistic effect between enzalutamide and a specific drug, while an SI score between 0.12 and 1 suggests a strong synergy. The results showed that 11 drugs in Hs578T and 23 drugs in BT549 cells had strong synergistic effects with enzalutamide (Fig. 1B). Moreover, seven drugs, including MK-8776, Ro-3306, CCT245737, KRpep-2d, CCT129202, CCT137690, and EHop-016, displayed potential synergistic effects with enzalutamide in both Hs578T and BT549 cells (Fig. 1C). Among them, MK-8776 has the relatively high and stable value in both Hs578T and BT549 cells (0.37 in Hs578T, 0.33 in BT549) compared with other agents (Fig. 1D).

3.2. Characterization of the anti-TNBC impact of the combined use of enzalutamide and MK-8776

CCK-8 assay was utilized to validate the synergism of MK-8776 (Fig. 2A) and six other agents (Supporting Information Figs. S3A and S3B) in combination with enzalutamide further. CHK1, an important cell cycle checkpoint kinase responsible for the regulation of the cell cycle and DNA damage response, is tightly involved in the progression of TNBC[32,33]. Thus, MK-8776, the typical inhibitor of CHK1, was selected for further study owing to its stable value and significant synergism with enzalutamide in both Hs578T and BT549 cells. Subsequently, the cell viability of Hs578T and BT549 cells treated with a 5-by-5 dose titration matrix of enzalutamide and MK-8776 was used to calculate the drug combination index (CI). When the CI value is under 1.0, it is considered to have a combined effect. In the Fa-CI plots, the majority of the dots (each dot represents a combination of a particular concentration of two drugs) had a CI value below 1.0 (Fig. 2B), indicating that enzalutamide and MK-8776 interacted in a synergistic manner. Moreover, we employed typical synergy models (HSA and Bliss) to estimate the HSA and Bliss values, which are a readout for synergistic inhibition and show the discrepancy between expected and observed inhibition[31,34]. The majority of the HSA and Bliss values exceeded 0, showing that the two drugs interacted synergistically (Fig. 2C). These data confirmed that the two agents' combination had a greater inhibitory effect on TNBC cell proliferation than either treatment alone produced in various models.

3.3. Enzalutamide and MK-8776 synergistically inhibited TNBC cell viability and migration

CHK1 is a serine/threonine-protein kinase that is responsible for the activation of cell cycle checkpoints, and MK-8776 is an important and selective inhibitor of CHK1. Based on this, we assumed that the synergy of the two agents might be involved in the regulation of the cell cycle. Using flow cytometry assays, we observed that more cells were blocked in the G2/M phase in the combined use of enzalutamide and MK-8776 group than in the

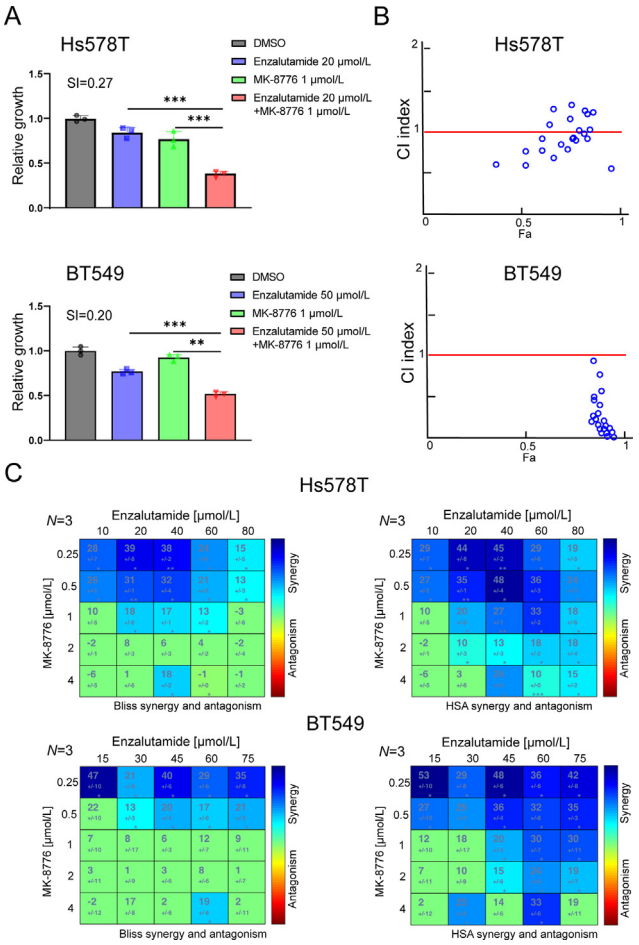

Figure 2 Characterization of the anti-TNBC impact of the combined use of enzalutamide and MK-8776. (A) The viability of Hs578T and BT549 cells treated with enzalutamide, MK-8776, or both was detected by CCK-8. (B) Analysis of the interaction between enzalutamide and MK-8776 and the resulting Fa-CI plots (fraction affected combination Index). (C) Combeneft-created synergy graphs displaying the interaction of enzalutamide and MK-8776. HSA (high single agent) values and bliss values from the interaction analysis showed synergistic efficacy based on predicted and actual growth suppression. Values over 0 for HSA and bliss imply synergistic effects. Data are presented as mean ± SD ($n = 3$), $^{*}P < 0.05$, $^{**}P < 0.01$, $^{***}P < 0.001$.

control, enzalutamide, or MK-8776 groups (Fig. 3A and B). The arrest of the cell cycle might, in turn, contribute to massive cell apoptosis. We found that the combination of enzalutamide and MK-8776 aggravated cell apoptosis compared to the mono-drug groups (Fig. 3C and D). In addition, the combination group exhibited increased BAX expression but decreased BCL-2 expression (Supporting Information Figs. S4A and S4B). Apart from checkpoint activation, CHK1 is involved in the DNA damage response by the homologous recombinational repair (HRR) pathway[35]. In order to explore the influence of the drug combination on DNA damage, we detected the expression of the DNA damage marker protein γ-H2AX. As the results showed, the single application of enzalutamide had little effect on the expression of γ-H2AX, while the treatment of MK-8776 promoted it. Interestingly, the combination of enzalutamide and MK-8776 accelerated the most protein expression of γ-H2AX in TNBC cells (Fig. 3E and F). The damage to DNA activates the DNA damage repair pathway, which is associated with repair proteins, including RAD50, RAD51, and DNA-PKcs. No matter whether the drugs were used alone or in combination, the protein expression of RAD50 and DNA-PKcs was not changed obviously, whereas the expression of RAD51 was reduced remarkably in the combination group (Fig. 3E and F). Moreover, the introduction of RAD51 in the combination group, however, reversed the synergism on DNA damage of drugs by elevating the expression of RAD51 and reducing γ-H2AX expression levels (Supporting Information Fig. S5A and S5B). These results indicated that the combination of MK-8776 and enzalutamide might exert a synergistic role by inhibiting the expression of RAD51, enhancing DNA damage, and subsequently inducing more apoptosis in TNBC cells.

Due to TNBC being aggressive and metastatic, repressing the invasion and distant metastasis of tumor cells holds crucial therapeutic importance. Transwell and wound healing assays were used to clarify the combined effect of enzalutamide and MK-8776 on cell migration and invasion. The Transwell assay revealed that the combination group significantly suppressed cell migration (Fig. 4A and B) and invasion (Fig. 4C and D) compared to the control group and monotherapy groups. Meanwhile, the migrated ability of TNBC cells was also determined by wound healing assay, and the results shared a similar trend with the Transwell assay (Fig. 4E and F). The expression of migration-related proteins, such as MMP-9, MMP-2, Vimentin, and E-cadherin, was further detected. Enzalutamide or MK-8776 application restrained MMP-9, MMP-2, and Vimentin expression while enhancing E-cadherin expression. However, their combined application exhibited more pronounced alterations in their expression levels (Fig. 4G and H). This suggests that the combination of enzalutamide and MK-8776 may more effectively inhibit tumor cell invasion and metastasis by modulating MMP-9, MMP-2, Vimentin, and E-cadherin expression levels. These findings revealed that the combination of enzalutamide and MK-8776 repressed the migration and invasion of TNBC cells more effectively than a single agent, confirming their synergistic effects.

3.4. Characterization and efficacy of HMnE&M@H nanoparticles

Although the combination of enzalutamide and MK-8776 has shown good anti-tumor effects in TNBC, the simple addition of two agents usually leads to inconsistent drug distribution, undermining treatment efficiency *in vivo*[36]. In order to resolve this problem, nanomaterials capable of preferential accumulation in tumors through the enhanced permeability and retention (EPR) effect were introduced to reduce off-target effects on other tissues and organs. Hollow MnO_2 ($HMnO_2$, also known as HMn), characterized by a hollow structure with pores on the surface responsible for drug loading, reacts with glutathione (GSH) in the acidic TME. This reaction leads to its degradation into Mn^{2+}, subsequently facilitating drug release. $HMnO_2$ was used to simultaneously load enzalutamide and MK-8776 for drug delivery[29]. Firstly, monodisperse silica nanoparticles with a diameter of about 60 nm were synthesized (Fig. 5A) and coated with a common reducing agent, polydopamine (Fig. 5B). Subsequently, oxidation by $KMnO_4$ generated a layer of MnO_2, eventually leading to the production of $HMnO_2$ through sodium hydroxide etching (Fig. 5C). X-ray photoelectron spectroscopy (XPS) was used to identify the main constituents in order to further confirm the validity of $HMnO_2$ nanoparticles. As XPS analysis showed,

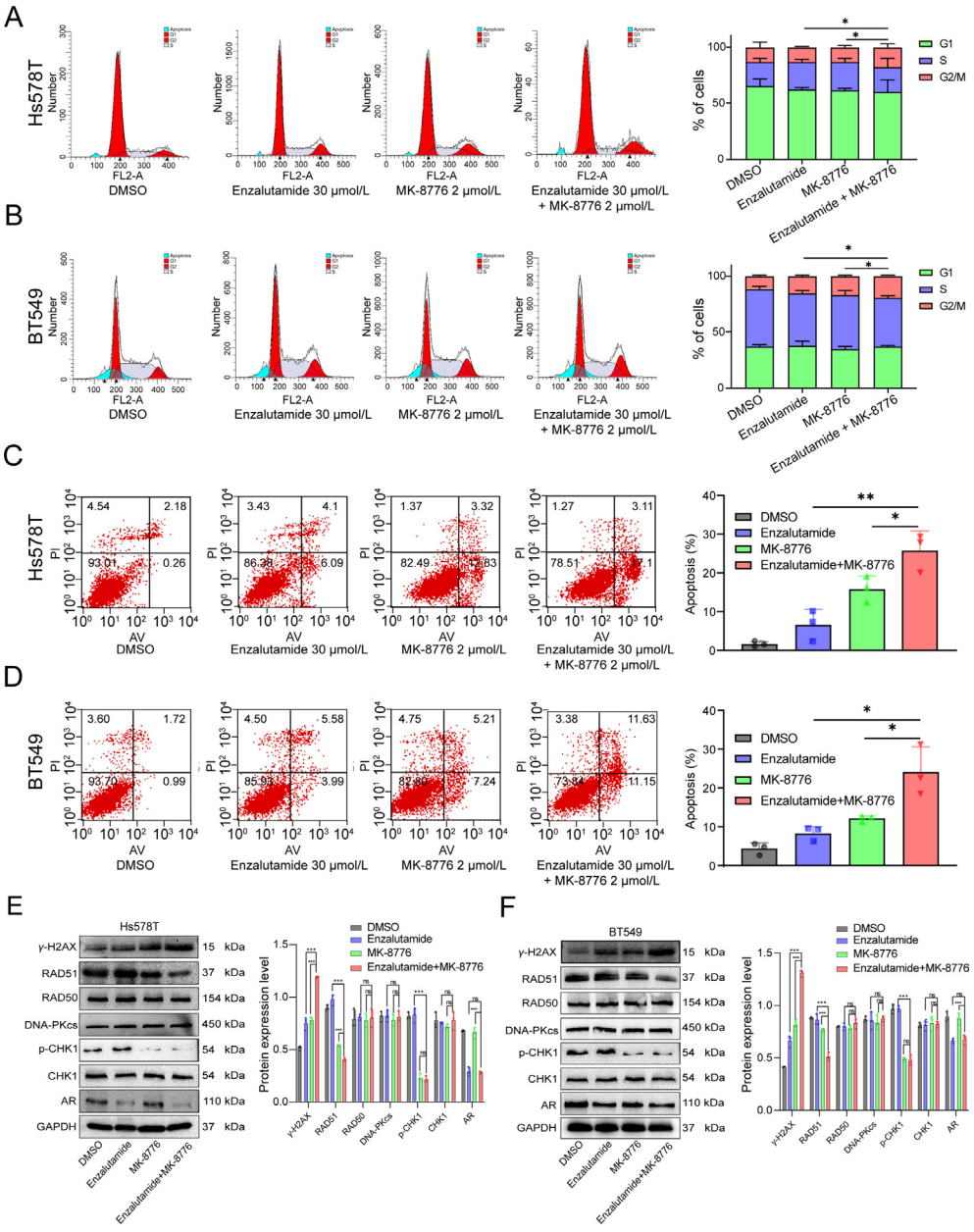

Figure 3 The combination of enzalutamide and MK-8776 synergistically induces cycle arrest, apoptosis, and DNA damage. (A) and (B) Flow cytometry analysis of the percentage of the cell cycle of Hs578T and BT549 cells after pretreatment with enzalutamide, MK-8776, or both for 24 h. (C) and (D) Flow cytometry analysis of the proportion of apoptotic Hs578T and BT549 cells treated for 24 h with enzalutamide, MK-8776, or both. (E) and (F) The protein expression of CHK1, p-CHK1, AR, DNA damage-related protein (γ-H2AX), and DNA damage repair-related proteins (RAD51, RAD50, and DNA-PKcs) in Hs578T and BT549 cells treated with indicated agents (DMSO, enzalutamide 30 μmol/L, MK-8776 2 μmol/L, and enzalutamide 30 μmol/L + MK-8776 2 μmol/L). Data are presented as mean ± SD ($n = 3$), $^{*}P < 0.05$, $^{**}P < 0.01$, $^{***}P < 0.001$; ns, not significant.

$HMnO_2$ revealed a spin energy span of 11.7eV between Mn (IV) 2p3/2 and Mn (IV) 2p1/2 (Fig. 5D), indicating the +4-valence state of manganese in the nanoparticles. The nitrogen adsorption results showed that the average pore size of $HMnO_2$ is 5.12 nm (Fig. 5E), indicating that the synthesized $HMnO_2$ has a larger specific surface area and is an appropriate carrier for drug delivery. HA coating can specifically improve the stability and targeting ability of nanomaterials; thus, it has been linked to the $HMnO_2$ surface (termed as HMn@H)[37,38]. The change of average Zeta potentials of MnO_2, HMnE&M, and HMnE&M@H (−19.27, −15.80, and −23.23 mV) indicated the successful loading of the drugs and the encapsulation by HA (Supporting Information Fig. S6A). The HMnE&M@H hydrodynamic size was slightly larger than $HMnO_2$ before loading (Figs. S6B and S6C) as measured by dynamic light scattering (DLS). In addition, we investigated the stability of HMnE&M@H in various media (saline, PBS, and medium containing 10% FBS), and the diameter of it remained unchanged during 72 h (Fig. S6D), suggesting its stability. Furthermore, low hemolysis rates were verified for HMnE&M@H (Supporting Information Fig. S7), indicating its

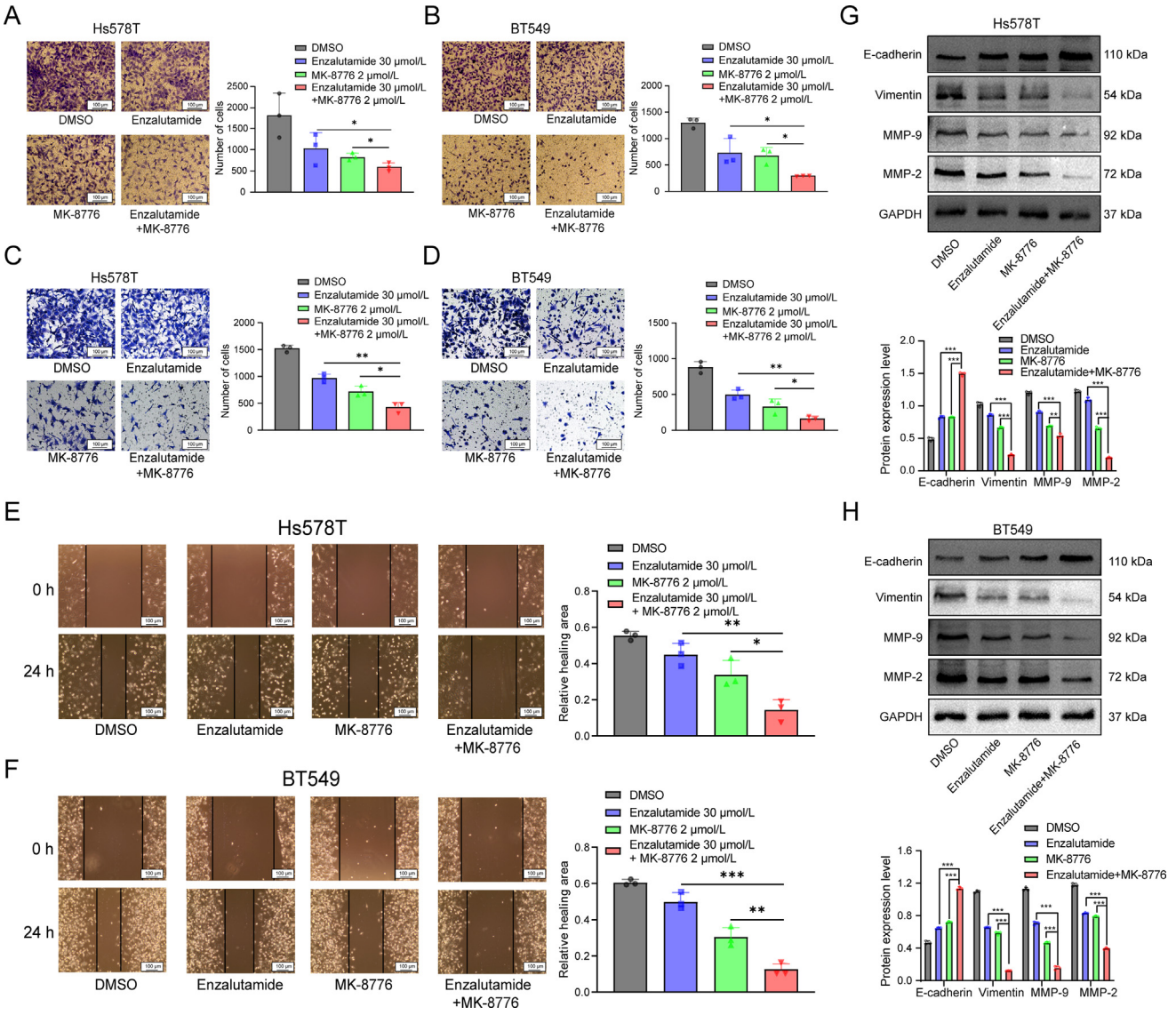

Figure 4 Enzalutamide and MK-8776 synergistically inhibited TNBC cell migration and invasion. (A) and (B) Transwell assays were utilized to examine the migratory capabilities of Hs578T and BT549 cells after the treatment of enzalutamide, MK-8776, or enzalutamide and MK-8776. (C) and (D) The cell invasion of Hs578T and BT549 cells was detected using a transwell assay. (E) and (F) The scratch wound assay was applied to examine the cell migration in indicated groups of Hs578T and BT549 cells. (G) and (H) The expression of E-cadherin, Vimentin, MMP-9, and MMP-2 in indicated groups (DMSO, enzalutamide 30 μmol/L, MK-8776 2 μmol/L, and enzalutamide 30 μmol/L + MK-8776 2 μmol/L) of both cell lines. Scale bar = 100 μm. Data are presented as mean ± SD ($n = 3$), $^{*}P < 0.05$, $^{**}P < 0.01$, $^{***}P < 0.001$.

excellent blood compatibility. The optimal mass ratios of $HMnO_2$ to enzalutamide (1:2) and $HMnO_2$ to MK-8776 (1:4) were determined to achieve the highest drug loading ratios of 59.4% and 54.1%, respectively, as demonstrated by the supernatant assay (Fig. 5F). In PBS (pH 7.4), negligible drug release was detected within 12 h. However, in the presence of 10 mmol/L GSH (pH 5.5), 88.5% enzalutamide and 92.3% MK-8776 were released, indicating pH/GSH-responsive drug release (Fig. 5G). Besides, HA coating did not significantly influence the drug release efficiency of HMnE&M@H (Supporting Information Fig. S8). $HMnO_2$ labeled with Cy7 (HMn@H-Cy7) was applied to evaluate the uptake of $HMnO_2$ by TNBC cells. Confocal microscopy confirmed the absorption of HMn@H-Cy7 by Hs578T, BT549, and 4T1 cells, indicating the potential of $HMnO_2$ as a delivery vehicle (Fig. 5H). Additionally, flow cytometry using labeled Cy7 fluorescent signals demonstrated higher absorption of HMnE&M@H by TNBC cells compared to HMnE&M (Supporting Information Fig. S9A–S9C), confirming enhanced tumor-targeting ability with HA-coated nanoparticles. Moreover, in the MTT assay, HMnE&M@H demonstrated stronger cytotoxic effects than HMnE&M (Supporting Information Fig. S10A–S10C), suggesting that HA coating might augment the cytotoxicity of nanoparticles. We measured the cell viability of Hs578T, BT549, and 4T1 cells following treatment with HMnE@H, HMnM@H, or HMnE&M@H. Among these, HMnE&M@H demonstrated greater lethality in tumor cells compared to the other groups, and the SI scores were all above 0.12 (Fig. 5I). This highlights the synergistic effects of HMnE&M@H. Additionally, the direct combination of enzalutamide and MK-8776 also attenuated TNBC cell viability; however,

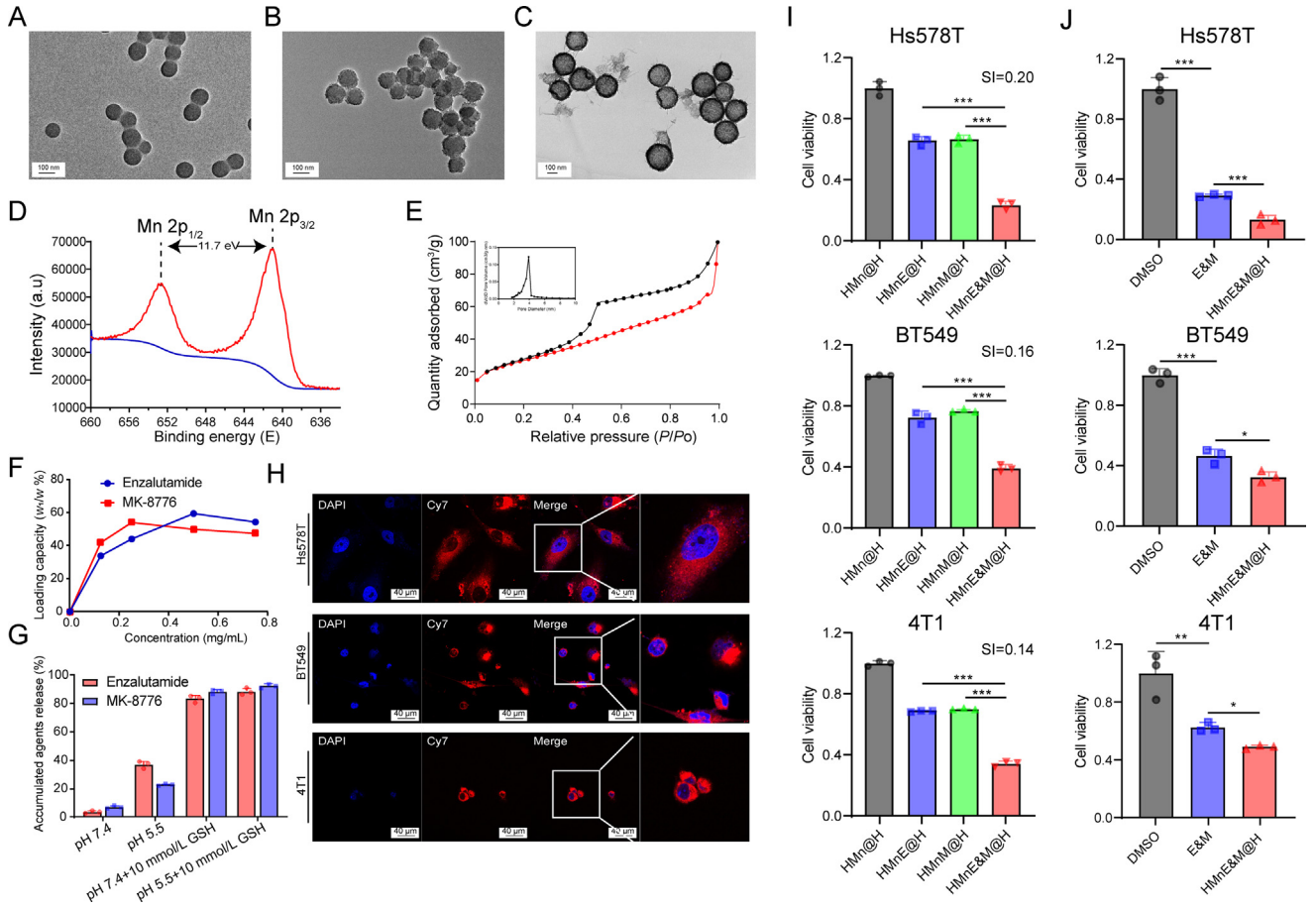

Figure 5 Characterization and efficacy of HMnE&M@H nanoparticles. TEM images of SiO_2 (A), SiO_2@PDA@MnO_2 (B), and $HMnO_2$ (C) nanoparticles. Scale bar = 100 nm. (D) XPS analysis of $HMnO_2$ nanoparticles. (E) BET analysis of $HMnO_2$ nanoparticles. (F) Quantification of enzalutamide and MK-8776 loadings at different concentrations. (G) Percentages of released enzalutamide and MK-8776 from HMnE and HMnM, respectively, in different conditions after 12 h. (H) Confocal images of three TNBC cell lines treated with HMn@H-Cy7. Blue represents DAPI, and red represents Cy7 fluorescence. Scale bar = 40 μm. (I) Cell viability and SI scores of Hs578T, BT549 and 4T1 cells treated with $HMnO_2$@H, HMnE@H (30 μmol/L enzalutamide), HMnM@H (2 μmol/L MK-8776), and HMnE&M@H (30 μmol/L enzalutamide + 2 μmol/L MK-8776). (J) Cell viability of TNBC cells treated with simple drug combination E&M (30 μmol/L enzalutamide + 2 μmol/L MK-8776) and HMnE&M@H (30 μmol/L enzalutamide + 2 μmol/L MK-8776). Data are presented as mean ± SD (n = 3), *P < 0.05, **P < 0.01, ***P < 0.001.

the treatment of HMnE&M@H, which was fabricated by using $HMnO_2$ to load them simultaneously, had a stronger anti-tumor effect (Fig. 5J). As shown in Supporting Information Fig. S11A and S11B, treatment with HMnE&M@H induced the most severe apoptosis in Hs578T and BT549 cells, indicating the fabulous tumor-suppressing effects of HMnE&M@H. The influence of nanoparticles on the DNA damage response was also examined. With the treatment of HMnE&M@H, the level of DNA damage marker protein γ-H2AX was elevated more significantly than the E&M-treated group, while other groups had little γ-H2AX expression. Notably, the DNA damage repair marker protein RAD51 level was reduced obviously in the HMnE&M@H-treated group, suggesting that HMnE&M@H might exert its anti-tumor role by promoting DNA damage and inhibiting the DNA repair process (Supporting Information Fig. S12A and S12B).

3.5. *In vivo anti-tumor effects of HMnE&M@H*

In order to estimate the anti-tumor effects of this nanoparticle, its biodistribution was detected first. With the treatment of HMnE&M@H-Cy7, it can be seen that the Cy7 fluorescence signals are mainly enriched within the tumor region at 1, 4, 8, and 24 h. In the HMnE&M-Cy7 group, the fluorescence signals can be observed in tumors; however, they were also widely present in other regions, especially at 1, 4, and 8 h (Fig. 6A). Despite $HMnO_2$ reaching tumors through the EPR effect, it also spread widely to other regions. The HA modification significantly improved the tumor targeting of the nanoparticle, leveraging HA's capacity to target CD44 in tumors[39]. Subsequently, after 24 h, the primary organs were harvested to observe the distribution of nanoparticles. As shown in Fig. 6B, HMnE&M@H-Cy7 was accumulated in the tumor more obviously than HMnE&M-Cy7. Inductively coupled plasma (ICP) was applied to analyze the biodistribution of Mn in the tumor and primary organs. It was found that Mn aggregated not only in the tumor but also in the liver, lung, and kidney (Supporting Information Fig. S13), which might reflect the metabolic pathways of nanomaterials. Owing to the outstanding imaging capability of $HMnO_2$ in the magnetic resonance imaging (MRI) system, the accumulation of HMnE&M@H in the tumor location was easily detected by MRI after intravenous injection. As shown in Fig. 6C, prior to the

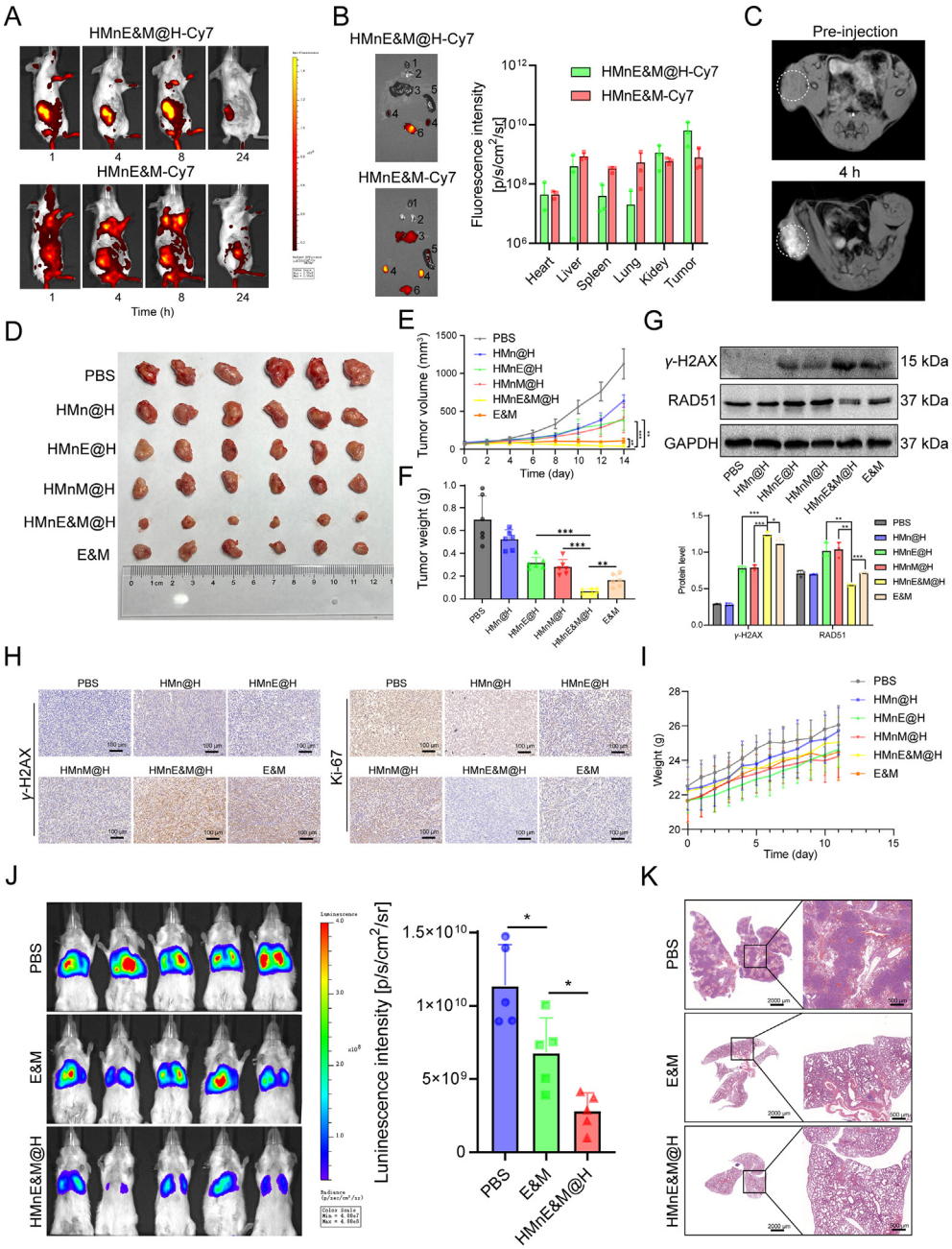

Figure 6 *In vivo* anti-tumor effects of HMnE&M@H. (A) and (B) *In vivo* and *ex vivo* (1: heart; 2: lung; 3: liver; 4: kidney; 5: spleen; 6: tumor) fluorescence images of 4T1 tumor-bearing mice taken at different time points post intravenous injection of HMnE&M@H-Cy7 and HMnE&M-Cy7. (C) *In vivo* T1-weighted MR images after intravenous injection with HMnE&M@H nanoparticles. (D) Tumor size, (E) Tumor volume, and (F) Tumor weight of each treatment group. Data are presented as mean ± SD ($n = 6$), $^{**}P < 0.01$, $^{***}P < 0.001$. (G) The protein expression of γ-H2AX and RAD51 of subcutaneous tumor after various treatments. Data are presented as mean ± SD ($n = 3$), $^{*}P < 0.05$, $^{**}P < 0.01$, $^{***}P < 0.001$. (H) The expression of Ki-67 and γ-H2AX of subcutaneous tumor in each group. Scale bar = 100 μm. (I) The body weight of mice in each treatment group. (J) and (K) Bioluminescence imaging and HE staining revealed that HMnE&M@H inhibited lung metastasis of circulating 4T1 cells. Left: Scale bar = 2000 μm, Right: Scale bar = 500 μm. Data are presented as mean ± SD ($n = 5$), $^{*}P < 0.05$.

injection of the nanoagent, the tumor area showed signal intensity similar to that of the adjacent tissues on T1-weighted imaging. However, T1-weighted imaging of the tumor area was significantly enhanced after the intravenous injection of HMnE&M@H. This phenomenon directly demonstrated the absorption of HMnE&M@H by tumors and highlighted the potential application of manganese dioxide nanoshells for tumor-specific imaging.

Subsequently, the mice were divided into six distinct treatment groups randomly (PBS, HMn@H, HMnE@H, HMnM@H, HMnE&M@H, and enzalutamide and MK-8776 (E&M)), and were treated every other day for two weeks. Tumor weight and size were assessed. The HMnE&M@H group demonstrated the most significant suppression of tumor growth compared to the groups receiving HMnE@H, HMnM@H, or the two-drug

combination (Fig. 6D−F), highlighting the outstanding anti-tumor effect of HMnE&M@H *in vivo*. In order to verify whether the nanoparticles HMnE&M@H can effectively stabilize the carried drugs and accurately deliver both drugs to tumor tissues at the intended 1:4 ratio (MK-8776: enzalutamide), we detected the drug concentrations in tumor tissues after the treatment with HMnE&M@H. The dose of MK-8776 was around 76.05 mg/kg, and enzalutamide was approximately 324.76 mg/kg (Supporting Information Fig. S14), resulting in a ratio of 1:4.27 (MK-8776: enzalutamide), close to our designed 1:4 ratio. Accordingly, HMnE&M@H can effectively stabilize the carried drugs and accurately deliver both drugs to tumor tissues at the intended ratio *in vivo*. The influence of HMnE&M@H on DNA damage was also detected in tumor tissues, and HMnE&M@H most effectively resulted in the increase of γ-H2AX and reduction of RAD51 (Fig. 6G). IHC results indicated that HMnE&M@H caused the most significant DNA damage compared to other groups and most effectively inhibited the expression of proliferation marker Ki-67 (Fig. 6H). Notably, the change in mice weight was similar between the HMnE&M@H and control groups, suggesting the safety of the nanoparticles (Fig. 6I). In addition, healthy mice injected with HMnE&M@H were sacrificed for blood collection at 0 (applied as a control), 1, 3, and 7 days to detect biochemical indexes, including alkaline phosphatase (ALP), alanine aminotransferase (ALT), aspartate aminotransferase (AST), creatinine (CREA), total protein (TP), and urea nitrogen (UREA) levels. No significant differences were discovered (Supporting Information Fig. S15). These findings indicate that HMnE&M@H has little toxic effect on liver and kidney function. Besides, HE assays showed no obvious pathological changes in primary organs after the indicated treatments (Supporting Information Fig. S16), suggesting the biosafety of HMnE&M@H. We then investigated whether HMnE&M@H could serve as a therapeutic approach for metastatic TNBC cells. Murine models of breast cancer lung metastasis were established *via* tail-vein injection of 4T1-luc cells. Mice were treated with PBS, E&M, and HMnE&M@H. Bioluminescence imaging of the lung indicated the *in vivo* metastatic potential of 4T1 cells. Reduced ROI values were observed in the lungs with 4T1-luc metastasis in the E&M group treated with a simple combination of two drugs, while the reduction was more pronounced in the HMnE&M@H group (Fig. 6J). Subsequently, lung tissues were harvested, and HE staining was conducted to visualize metastatic sites (Fig. 6K). The lung metastasis model demonstrated that HMnE&M@H significantly impaired the metastasis of circulating cancer cells. Collectively, the nanoparticle HMnE&M@H is a very promising targeted drug for TNBC therapy due to its excellent anti-tumor effects and minimal side effects *in vivo*.

4. Discussion

Identifying druggable biomarkers and improving targeting activity has been a crucial pursuit in the field of oncology. Breast cancer has risen to be the malignancy with the highest female morbidity globally; however, hormone therapy and anti-HER2 treatment have proven efficacious for a majority of breast cancer patients. Nevertheless, chemotherapy remains the foundation and even the only choice for most TNBC patients. The lack of treatment options for TNBC easily contributes to quicker chemotherapy resistance and side effects because of increased drug dosages. Thus, there is an urgent need to identify novel prospective targets for this targetless breast cancer subtype and establish effective delivery to the tumor sites.

Our previous research demonstrated that androgen was the potential modulator in the proliferation and progression of AR-positive breast cancer cell lines[40,41]. A phase II clinical trial MDV3100-11 demonstrated clinical activity and good tolerance of androgen inhibition among AR-positive TNBC patients; however, over 80% of participants discontinued because of disease progression[20]. The above reports suggested the efficacy of anti-AR as well as the demand to synergize the clinical efficacy of anti-AR-based regimens. Some preclinical data have revealed that AR is associated with various intracellular signaling pathways, including cell cycle pathways and multiple key proteins, such as BRCA1 and BRCA2. After summarizing the biological functions of these key proteins, we concluded that cell cycle regulation might be the pivotal mechanism by which AR influences the growth and progression of AR-positive TNBC[41]. Therefore, we performed screening on cell cycle drugs to identify the specific agents that synergize with enzalutamide to enhance its anti-cancer effects. In the current research, we revealed that the selective CHK1 inhibitor MK-8776 has strong synergistic effects with enzalutamide in TNBC cells by aggravating cell apoptosis and inhibiting cell migration and invasion. CHK1 is the core protein of cell cycle checkpoints. Its deficiency renders tumor cells more sensitive to radiotherapy and chemotherapy[42,43]. Some reports have demonstrated that CHK1 inhibitors have a "synthetic lethal" effect when combined with other small-molecule targeted drugs[44,45]. Furthermore, compared to non-TNBC tissues, CHK1 is markedly upregulated in TNBC tumor tissues[46]. Therefore, targeting CHK1 by MK-8776 in TNBC might be a convincing strategy to increase the efficacy of enzalutamide.

DNA damage response (DDR) is a term for a coordinated cellular mechanism that mitigates DNA damage accumulation and protects genomic integrity[47]. Moreover, DDR also exerts a critical role in the initiation and development of TNBC[48]. In DDR, CHK1 is a key signal sensor triggering cell cycle checkpoint activation. Besides, CHK1-mediated checkpoints can lead to the resistance of tumor cells to the cytotoxicity of chemotherapy. Thus, CHK1 inhibitors have been developed as chemical sensitizers to boost the cytotoxicity of agents[49]. Interestingly, we found the combination of enzalutamide and MK-8776 induced the most DNA damage, while the treatment of enzalutamide caused minor damage. However, the DNA damage repair protein RAD51 was downregulated obviously in the combination group. This may explain why the application of enzalutamide only triggered slight DNA damage but was reversed thoroughly by the combination of MK-8776. From these results, we speculated that the improved DNA damage repair progression might be responsible for the resistance of AR inhibition (such as enzalutamide) in AR^{+}TNBC patients, whereas targeting CHK1 (such as MK-8776) could abolish it and lead to the tumor suppression of TNBC.

Nevertheless, drug combination therapy based on the simple addition of two preparations usually leads to inconsistent drug distribution *in vivo* and affects treatment efficiency due to the unique pharmacokinetic characteristics, biological interference, and membrane transport characteristics of different drug molecules. Therefore, simultaneous encapsulation of different drugs within nanomaterials has garnered significant attention. Different from organic nanoparticles, such as PLGA and liposome, inorganic nanoparticle MnO_2 has attracted substantial attention owing to their stronger mechanical stability and multiple unique advantages. MnO_2 is a TME-specific responsive nanoparticle, as it undergoes

degradation through reactions with either H^+ or GSH present within the TME, thus enhancing its tumor-targeting capability. Meanwhile, MnO_2 nanoparticles have high biosafety without long-term toxicity concerns[50,51]. It can be decomposed into water-soluble Mn^{2+} *in vivo* and then metabolized by the kidneys. TME is always hypoxia. However, MnO_2 nanoparticles can induce the decomposition of H_2O_2 within the TME into oxygen and water, thus improving the hypoxic environment and inhibiting tumor growth[51,52]. In addition, MnO_2 has a great advantage in imaging ability relying on the Mn^{2+} ions decomposed from them, which are able to enhance the T1-magnetic resonance imaging (MRI) and then improve specific imaging and detection for tumor region[53,54]. In light of that, for better *in vivo* application, we developed a new HMnE&M@H nano platform based on $HMnO_2$ nanoshells to load enzalutamide and MK-8776 simultaneously. This nanoparticle could stabilize its cargoes *in vivo* and release enzalutamide and MK-8776 accurately in the tumor region, thus improving the targeting and efficacy of the drug combination.

5. Conclusions

In summary, our findings demonstrated the synergistic anti-tumor effect of enzalutamide and MK-8776 in AR^+TNBC by using the drug combination screening method. Based on the screening results, we developed a nanoparticle (HMnE&M@H) simultaneously loaded with enzalutamide and MK-8776 to manage precise medication in the tumor site, thus improving the efficacy and targeting of the drug combination. Therefore, applying the drug combination screening method to screen out synergistic agent combinations and subsequently using appropriate materials, such as nanomaterials, for their encapsulation may represent a viable strategy for developing novel anti-tumor drugs. Consequently, our study constructed a nano drug delivery system HMnE&M@H as a potential therapeutic strategy for the targeted therapy of AR^+TNBC patients.

Acknowledgments

This study was supported by the Key INTERNATIONAL COOPERATION of the National Natural Science Foundation of China (No. 81920108029, China) and the Key Foundation for Social Development Project of the Jiangsu Province, China (No. BE2021741, China).

Author contributions

Xiaoxiang Guan and Xin Han conceived the idea and designed the experiments. Fangyan Gao, Yueyao Wu, and Runtian Wang performed the majority of the experimental work. Yuhui Yao, Yiqiu Liu, Lingling Fan, and Jingtong Xu performed the *in vivo* experiments. Fangyan Gao and Runtian Wang wrote the manuscript. Xiaoxiang Guan, Xin Han, and Jian Zhang supervised the project.

Conflicts of interest

The authors have no conflicts of interest to declare.

Appendix A. Supporting information

Supporting data to this article can be found online at https://doi.org/10.1016/j.apsb.2024.03.012.

References

1. Siegel RL, Miller KD, Fuchs HE, Jemal A. Cancer statistics. *CA Cancer J Clin* 2022;**72**:7−33. 2022.
2. Yin L, Duan JJ, Bian XW, Yu SC. Triple-negative breast cancer molecular subtyping and treatment progress. *Breast Cancer Res* 2020;**22**:61.
3. Echeverria GV, Powell E, Seth S, Ge Z, Carugo A, Bristow C, et al. High-resolution clonal mapping of multi-organ metastasis in triple negative breast cancer. *Nat Commun* 2018;**9**:5079.
4. Vagia E, Mahalingam D, Cristofanilli M. The landscape of targeted therapies in TNBC. *Cancers* 2020;**12**:916.
5. Echeverria GV, Ge Z, Seth S, Zhang X, Jeter-Jones S, Zhou X, et al. Resistance to neoadjuvant chemotherapy in triple-negative breast cancer mediated by a reversible drug-tolerant state. *Sci Transl Med* 2019;**11**:eaav0936.
6. Garrido-Castro AC, Lin NU, Polyak K. Insights into molecular classifications of triple-negative breast cancer: improving patient selection for treatment. *Cancer Discov* 2019;**9**:176−98.
7. Keung MY, Wu Y, Badar F, Vadgama JV. Response of breast cancer cells to PARP Inhibitors is independent of BRCA status. *J Clin Med* 2020;**9**:940.
8. Hu J, Shen Y, Zhang G, He J, Sun M, Zhang H, et al. Effect of acupoint therapies on chemotherapy-induced nausea and vomiting: a systematic review protocol. *Medicine (Baltimore)* 2019;**98**:e17109.
9. Li S, Chen J, Wang Y, Zhou X, Zhu W. Moxibustion for the side effects of surgical therapy and chemotherapy in patients with gastric cancer: a protocol for systematic review and meta-analysis. *Medicine (Baltimore)* 2020;**99**:e21087.
10. Barton VN, D'Amato NC, Gordon MA, Christenson JL, Elias A, Richer JK. Androgen receptor biology in triple negative breast cancer: a case for classification as AR+ or quadruple negative disease. *Horm Cancer* 2015;**6**:206−13.
11. Thorek DLJ, Ku AT, Mitsiades N, Veach D, Watson PA, Metha D, et al. Harnessing androgen receptor pathway activation for targeted alpha particle radioimmunotherapy of breast cancer. *Clin Cancer Res* 2019;**25**:881−91.
12. Gerratana L, Basile D, Buono G, De Placido S, Giuliano M, Minichillo S, et al. Androgen receptor in triple negative breast cancer: a potential target for the targetless subtype. *Cancer Treat Rev* 2018;**68**:102−10.
13. Bianchini G, Balko JM, Mayer IA, Sanders ME, Gianni L. Triple-negative breast cancer: challenges and opportunities of a heterogeneous disease. *Nat Rev Clin Oncol* 2016;**13**:674−90.
14. Denkert C, Liedtke C, Tutt A, von Minckwitz G. Molecular alterations in triple-negative breast cancer-the road to new treatment strategies. *Lancet* 2017;**389**:2430−42.
15. Tesei A, Castoria G. Editorial: the androgen receptor in breast cancer. *Front Endocrinol* 2020;**11**:636480.
16. Gucalp A, Tolaney S, Isakoff SJ, Ingle JN, Liu MC, Carey LA, et al. Phase II trial of bicalutamide in patients with androgen receptor-positive, estrogen receptor-negative metastatic breast cancer. *Clin Cancer Res* 2013;**19**:5505−12.
17. Farrow JM, Yang JC, Evans CP. Autophagy as a modulator and target in prostate cancer. *Nat Rev Urol* 2014;**11**:508−16.
18. Loriot Y, Bianchini D, Ileana E, Sandhu S, Patrikidou A, Pezaro C, et al. Antitumour activity of abiraterone acetate against metastatic castration-resistant prostate cancer progressing after docetaxel and enzalutamide (MDV3100). *Ann Oncol* 2013;**24**:1807−12.
19. Scher HI, Fizazi K, Saad F, Taplin ME, Sternberg CN, Miller K, et al. Increased survival with enzalutamide in prostate cancer after chemotherapy. *N Engl J Med* 2012;**367**:1187−97.
20. Traina TA, Miller K, Yardley DA, Eakle J, Schwartzberg LS, O'Shaughnessy J, et al. Enzalutamide for the treatment of androgen receptor-expressing triple-negative breast cancer. *J Clin Oncol* 2018;**36**:884−90.
21. Bian L, Xu FR, Jiang ZF. Endocrine therapy combined with targeted therapy in hormone receptor-positive metastatic breast cancer. *Chin Med J (Engl)* 2020;**133**:2338−45.

22. Finn RS, Martin M, Rugo HS, Jones S, Im SA, Gelmon K, et al. Palbociclib and letrozole in advanced breast cancer. *N Engl J Med* 2016;**375**:1925−36.
23. Lanzino M, Sisci D, Morelli C, Garofalo C, Catalano S, Casaburi I, et al. Inhibition of cyclin D1 expression by androgen receptor in breast cancer cells-identification of a novel androgen response element. *Nucleic Acids Res* 2010;**38**:5351−65.
24. Wang Y, He X, Yu Q, Eng C. Androgen receptor-induced tumor suppressor, KLLN, inhibits breast cancer growth and transcriptionally activates p53/p73-mediated apoptosis in breast carcinomas. *Hum Mol Genet* 2013;**22**:2263−72.
25. Zhu YX, Jia HR, Pan GY, Ulrich NW, Chen Z, Wu FG. Development of a light-controlled nanoplatform for direct nuclear delivery of molecular and nanoscale materials. *J Am Chem Soc* 2018;**140**: 4062−70.
26. Kang Y, Li S. Nanomaterials: breaking through the bottleneck of tumor immunotherapy. *Int J Biol Macromol* 2023;**230**:123159.
27. Gao X, Li L, Cai X, Huang Q, Xiao J, Cheng Y. Targeting nanoparticles for diagnosis and therapy of bone tumors: opportunities and challenges. *Biomaterials* 2021;**265**:120404.
28. Gao F, Tang Y, Liu WL, Zou MZ, Huang C, Liu CJ, et al. Intra/-Extracellular lactic acid exhaustion for synergistic metabolic therapy and immunotherapy of tumors. *Adv Mater* 2019;**31**:e1904639.
29. Yang G, Xu L, Chao Y, Xu J, Sun X, Wu Y, et al. Hollow MnO_2 as a tumor-microenvironment-responsive biodegradable nano-platform for combination therapy favoring anti-tumor immune responses. *Nat Commun* 2017;**8**:902.
30. Bijnsdorp IV, Giovannetti E, Peters GJ. Analysis of drug interactions. *Methods Mol Biol* 2011;**731**:421−34.
31. Chen Z, Chen C, Zhou T, Duan C, Wang Q, Zhou X, et al. A high-throughput drug combination screen identifies an anti-glioma synergism between TH588 and PI3K inhibitors. *Cancer Cell Int* 2020;**20**: 337.
32. Al-Kaabi MM, Alshareeda AT, Jerjees DA, Muftah AA, Green AR, Alsubhi NH, et al. Checkpoint kinase1 (CHK1) is an important biomarker in breast cancer having a role in chemotherapy response. *Br J Cancer* 2015;**112**:901−11.
33. Grellety T, Callens C, Richard E, Briaux A, Velasco V, Pulido M, et al. Enhancing abiraterone acetate efficacy in androgen receptor-positive triple-negative breast cancer: CHK1 as a potential target. *Clin Cancer Res* 2019;**25**:856−67.
34. Di Veroli GY, Fornari C, Wang D, Mollard S, Bramhall JL, Richards FM, et al. Combenefit: an interactive platform for the analysis and visualization of drug combinations. *Bioinformatics* 2016;**32**: 2866−8.
35. Choi C, Cho WK, Park S, Shin SW, Park W, Kim H, et al. Checkpoint Kinase 1 (CHK1) inhibition enhances the sensitivity of triple-negative breast cancer cells to proton irradiation *via* RAD51 downregulation. *Int J Mol Sci* 2020;**21**:2691.
36. Xu Y, Yao Y, Wang L, Chen H, Tan N. Hyaluronic acid coated liposomes co-delivery of natural cyclic peptide RA-XII and mitochondrial targeted photosensitizer for highly selective precise combined treatment of colon cancer. *Int J Nanomed* 2021;**16**:4929−42.
37. Wei X, Senanayake TH, Warren G, Vinogradov SV. Hyaluronic acid-based nanogel-drug conjugates with enhanced anti-cancer activity designed for the targeting of CD44-positive and drug-resistant tumors. *Bioconjug Chem* 2013;**24**:658−68.
38. Poudel K, Banstola A, Tran TH, Thapa RK, Gautam M, Ou W, et al. Hyaluronic acid wreathed, trio-stimuli receptive and on-demand triggerable nanoconstruct for anchored combinatorial cancer therapy. *Carbohydr Polym* 2020;**249**:116815.
39. Mattheolabakis G, Milane L, Singh A, Amiji MM. Hyaluronic acid targeting of CD44 for cancer therapy: from receptor biology to nanomedicine. *J Drug Target* 2015;**23**:605−18.
40. Song W, Tang L, Xu Y, Sun Q, Yang F, Guan X. ERbeta1 inhibits metastasis of androgen receptor-positive triple-negative breast cancer by suppressing ZEB1. *J Exp Clin Cancer Res* 2017;**36**:75.
41. Shi Y, Yang F, Huang D, Guan X. Androgen blockade based clinical trials landscape in triple negative breast cancer. *Biochim Biophys Acta Rev Cancer* 2018;**1870**:283−90.
42. Qiu Z, Oleinick NL, Zhang J. ATR/CHK1 inhibitors and cancer therapy. *Radiother Oncol* 2018;**126**:450−64.
43. Wen Y, Hou Y, Yi X, Sun S, Guo J, He X, et al. EZH2 activates CHK1 signaling to promote ovarian cancer chemoresistance by maintaining the properties of cancer stem cells. *Theranostics* 2021;**11**:1795−813.
44. Klomp JE, Lee YS, Goodwin CM, Papke B, Klomp JA, Waters AM, et al. CHK1 protects oncogenic KRAS-expressing cells from DNA damage and is a target for pancreatic cancer treatment. *Cell Rep* 2021; **37**:110060.
45. Biegala L, Gajek A, Marczak A, Rogalska A. PARP inhibitor resistance in ovarian cancer: underlying mechanisms and therapeutic approaches targeting the ATR/CHK1 pathway. *Biochim Biophys Acta Rev Cancer* 2021;**1876**:188633.
46. Albiges L, Goubar A, Scott V, Vicier C, Lefebvre C, Alsafadi S, et al. CHK1 as a new therapeutic target in triple-negative breast cancer. *Breast* 2014;**23**:250−8.
47. Jackson SP, Bartek J. The DNA-damage response in human biology and disease. *Nature* 2009;**461**:1071−8.
48. Khozooei S, Lettau K, Barletta F, Jost T, Rebholz S, Veerappan S, et al. Fisetin induces DNA double-strand break and interferes with the repair of radiation-induced damage to radiosensitize triple negative breast cancer cells. *J Exp Clin Cancer Res* 2022;**41**:256.
49. Carrassa L, Damia G. Unleashing CHK1 in cancer therapy. *Cell Cycle* 2011;**10**:2121−8.
50. Pi F, Deng X, Xue Q, Zheng L, Liu H, Yang F, et al. Alleviating the hypoxic tumor microenvironment with MnO_2-coated CeO_2 nanoplatform for magnetic resonance imaging guided radiotherapy. *J Nanobiotechnology* 2023;**21**:90.
51. Chen Q, Feng L, Liu J, Zhu W, Dong Z, Wu Y, et al. Intelligent Albumin-MnO_2 nanoparticles as pH-/H_2O_2-responsive dissociable nanocarriers to modulate tumor hypoxia for effective combination therapy. *Adv Mater* 2016;**28**:7129−36.
52. Fan H, Yan G, Zhao Z, Hu X, Zhang W, Liu H, et al. A smart photosensitizer-manganese dioxide nanosystem for enhanced photodynamic therapy by reducing glutathione levels in cancer cells. *Angew Chem Int Ed Engl* 2016;**55**:5477−82.
53. Zhang M, Cao Y, Wang L, Ma Y, Tu X, Zhang Z. Manganese doped iron oxide theranostic nanoparticles for combined T1 magnetic resonance imaging and photothermal therapy. *ACS Appl Mater Interfaces* 2015;**7**:4650−8.
54. Fan W, Bu W, Shen B, He Q, Cui Z, Liu Y, et al. Intelligent MnO_2 nanosheets anchored with upconversion nanoprobes for concurrent pH-/H_2O_2-responsive UCL imaging and oxygen-elevated synergetic therapy. *Adv Mater* 2015;**27**:4155−61.